

Differentiating the Bonding States in Calcium Carbonate Polymorphs by Low-loss Electron-Energy-Loss Spectroscopy

Yao-Wen Yeh¹, Sobhit Singh¹, Guangming Cheng^{2*}, Nan Yao², Karin M. Rabe¹, David Vanderbilt¹, Philip E. Batson¹, Long Pan³, Guofeng Xu³ and Shiyu Xu^{3*}

¹Department of Physics and Astronomy, Rutgers University, Piscataway, NJ 08854, USA

²Princeton Materials Institute, Princeton University, Princeton, NJ 08544, USA

³Colgate Technology Center, 909 River Road, Piscataway, NJ 08854, USA

Corresponding authors: gcheng2@princeton.edu, shiyu_xu@colpal.com

Abstract

Calcium carbonate is one of the important building components in organisms, especially the two most common polymorphs, calcite and aragonite. Here, to understand the difference in bonding state, the two polymorphs are characterized by valence (low-loss) electron energy loss spectroscopy. It is found that the difference in Ca M_{23} edge originating from $3p$ to $3d$ states is consistent with the change of Ca-O bonds in the two studied polymorphs. Surprisingly, the measured Ca M_{23} edge is in qualitative agreement with the calculated partial density of states (PDOS) of Ca- d states in contrast to their L edges (from $2p$ to $3d$ states) which are strongly influenced by atomic multiplet effect (spin-orbit coupling). This is because the atomic multiplet effect is much reduced for the Ca $3p$ orbital, which permits the corresponding Ca M_{23} edge to be compared with the PDOS results. Our findings show insights that PDOS can potentially be used

to interpret the M_{23} edge of lighter $3d$ transition metals such as scandium, titanium, vanadium and chromium when such interpretation may not be achieved for their L edges.

Key Words: calcium carbonate; calcite; aragonite; bonding state; EELS; DFT

1. Introduction

Calcium carbonate (CaCO_3) is abundant and naturally occurring compounds and is one of the very important building blocks in our ecosystem, especially in the ocean. For example, CaCO_3 is found in biomineral structures such as nacre and sea urchin spicules [1-4] and plays an essential role in such structures' remarkable mechanical properties [5, 6]. Due to its unique physical and mechanical properties, researchers are not only developing biomimetic materials based on its biomineral structures [7-9] but also utilizing it as additives for the applications in our daily life such as abrasive additives in toothpaste to help remove plaque, debris and surface stains [10, 11]. There exist three polymorphs of CaCO_3 – calcite, aragonite, and vaterite [12]. However, only the first two are readily available due to their thermodynamic stability, and they are the subjects of this work. Although their microstructures are well characterized, there is still lack of study about the electronic structures related to the bonding state (valence) in the compounds. A comprehensive understanding of their electronic structure could help to further understand structurally influenced and controlled material properties.

Experimentally, the electronic structures of materials can be studied by electron energy loss spectroscopy (EELS) and X-ray absorption spectroscopy (XAS) [13]. Especially, low-loss EELS is indicative of outer-shell single electron transitions and collective excitations of valence electrons. For calcite and aragonite, the Ca L_2 and L_3 core edges around 345 eV represent transitions from the initial $2p$ to the final $3d$ states and are one of the effective means of characterizing calcite and

aragonite as their constituent atoms are arranged differently, yielding different crystal field effects [14-16]. However, similar to $3d$ transition metal compounds [17], the involvement of $2p$ to $3d$ states make the spectral features in the Ca- L edges strongly influenced by atomic multiplet effect (spin-orbit coupling) which makes difficult to interpret the core-loss EELS data [15]. Hence, the Ca L edges cannot provide us more information about the bonding states in the compounds. Fortunately, we found that Ca- M edges showed advantages for the analysis of bonding states in the two studied CaCO_3 polymorphs because the spin-orbit coupling is much reduced for a $3p$ orbital as compared to a $2p$ orbital, which in turn reduces the atomic multiplet effect. This enables us to deeply explore the fine spectral features (band gap, bonding states and dielectric function) from low-loss EELS data.

Here, we use scanning transmission electron microscopy (STEM) coupled with EELS to characterize the valence (low-loss) spectral region (4 – 50 eV) of calcite and aragonite. Within this energy range, we explore the Ca M_{23} edge starting around 26 eV to distinguish the bonding states in the two polymorphs and adopt *ab-initio* density-functional theory (DFT) calculations to interpret the measured spectra. This energy range offers two attractive advantages in EELS analysis. First, the signal intensity in the low-loss region is more than one order of magnitude stronger than that of the loss range above 100 eV [13], which allows fast spectrum acquisitions and can be beneficial when the materials of interest are electron-radiation sensitive as in the case of calcium carbonates [16, 18]. Second, it allows us to study the dielectric properties with a wider energy range than that by ultraviolet (UV) photons used in typical optical methods [6, 19], and provides the information to be useful for soft X-ray applications. Note that although Katti *et al.* and Srot *et al.* studied calcite and aragonite by using low-loss EELS, the primary objective of their work focused on the

difference of the two CaCO₃ polymorphs between their geological and biogenic forms but no detailed study of the spectral features [20, 21].

2. Materials and Methods

Calcium carbonate powder containing calcite and aragonite was obtained from Himachal Polyolefins Ltd. The electron microscopy samples were prepared by first mixing the powder in ethanol via sonication and then drop casting the sample containing solution on a lacey carbon coated grid.

2.1 Imaging and Spectroscopy Acquisitions

Conventional transmission electron microscope (TEM) imaging was performed on a Titan Cubed Themis 300 double Cs-corrected scanning/transmission electron microscope (S/TEM), equipped with an extreme field emission gun source and a super-X EDS system. The system was operated at 200 kV.

Both the STEM imaging and EELS acquisitions were carried out using a Nion UltraSTEM microscope operated at 60 kV with the convergence and collection semi-angles set at 30 mrad and 16.5 mrad, respectively. Note that Cherenkov radiation loss can be neglected in our collected low-loss EELS data by taking into account of the refractive indices of calcite and aragonite, 1.486-1.658 [22-25]. Both calcite and aragonite are electron beam sensitive materials. In order to minimize the electron beam damage to the materials and obtain spectra intrinsic to the materials, the spectra were acquired at -2 μm defocus while setting the electron probe under constant scanning motion with a nominal scan size of 32 by 32 nm.

Typical sample thickness for the collection of EELS data was around 0.7 of the effective inelastic mean free path of the incident electrons. Combining the measured mean free path and Lenz model [13, 26], the sample thickness was estimated to be around 56 nm. Single scattering

spectra were obtained by applying Fourier-log deconvolution [13] to the raw spectra. In order to balance the signal intensity and acquisition time for the valence loss experiments, a mildly monochromated electron probe was used with the energy resolution of 0.134 eV as determined by the full-width-at-half-maximum of the zero-loss peak. For the Ca *L* edge spectra reported here, the energy resolution is 0.242 eV. The procedures to obtain the dielectric functions of calcite and aragonite from the measured valence spectra are described in Appendix A and Appendix B. To remove the surface loss (typically for thin samples with thickness of less than 100 nm), the low-loss EELS data was processed by using Kramers–Kronig analysis [27-29].

2.2 *Ab-initio* DFT Calculations

The reported *ab-initio* DFT calculations were performed using the Projector Augmented Wave (PAW) method as implemented in the Vienna Ab initio Simulation Package (VASP) [30-32]. Eight, four, and six valence electrons were considered in the calcium, carbon, and oxygen PAW pseudopotentials, respectively. The Perdew-Bruke-Ernzerhof generalized-gradient approximation for solids (GGA-PBEsol) was used for the exchange-correlation functional [33]. The plane-wave energy cutoff was set to 600 eV. The energy convergence and force convergence criteria were set to 10^{-8} eV and 10^{-3} eV/Å, respectively. Although spin-orbit coupling (SOC) effects were found to be insignificant for the studied materials, they were included in the reported DFT results. The Pyprocar [34] package was utilized for the analysis of electronic band-structure.

For calcite, we considered a rhombohedral primitive unit cell (space group $R\bar{3}c$) consisting of 4 formula units in our DFT calculations (see Figure 4). The PBEsol-DFT optimized lattice parameters for calcite are $a = b = 4.993$, and $c = 16.802$ Å in the conventional unit cell setting, which compare reasonably well with the reported experimental data ($a = b = 4.988$, and $c = 17.068$ Å) [35]. In the case of aragonite (space group *Pmcn*), the PBEsol-DFT optimized lattice

parameters are $a = 4.944$, $b = 7.917$, and $c = 5.461$ Å, which are in good agreement with the reported experimental data ($a = 4.960$, $b = 7.964$, and $c = 5.738$ Å) [36].

3. Results and Discussion

Typical sample appearances are shown in Figure 1, where the calcite and aragonite particles exhibit rod-like and cube-like shapes, respectively. The diffraction patterns in Figures 1b and d confirmed that the particles are from calcite and aragonite, respectively. In addition to the particle shape difference, the Ca atom bonding environments in the two polymorphs are also different. In calcite, each Ca atom is enclosed by six oxygen atoms and the Ca-O bond angles are either 87.25° or 92.25° leading to the lower symmetry D_{3d} point group than the perfect octahedral arrangement (O_h) found in Ca oxide [15]. In aragonite, each Ca atom bonds with nine neighboring oxygen atoms, which forms a complex polyhedron showing a D_{2h} point group symmetry. Aragonite's D_{2h} point group has even lower symmetry than that of calcite. As will be discussed in more detail later, the crystal symmetry plays an important role in the resulting $3d$ states due to the crystal field effect.

3.1 Valence Electronic Structures

The valence loss spectra of calcite and aragonite shown in Figure 2 are the single-scattering spectra after Fourier-log deconvolution [13] with the intensity normalized to the total spectrum intensities. The spectra can roughly be broken down into two regions. The features below 26 eV involve the interband transitions between valence and conduction bands of the samples, while the features above 26 eV involve shallow core electron (Ca $3p$) transitions to the conduction bands (i.e. M edge).

We began our spectral analysis by examining the beginning of the loss spectra that contains band gap information. Both calcite and aragonite are wide band gap materials. Following Rafferty and Brown's EELS band gap analysis [37], we found that both calcite and aragonite have indirect

band gaps of 7.10 ± 0.14 and 6.79 ± 0.14 eV, respectively, based on the $(E - E_g)^{1.5}$ behavior around the onset of the spectra as indicated in Figure 3. Our DFT calculations (with SOC) predicted an indirect energy band gaps of 5.00 and 4.08 eV for calcite and aragonite (along the direction of blue arrow shown in Figure 4), respectively, which are consistent with previous reports [12, 38-41]. As is widely accepted, the DFT predicted band gaps are usually underestimated as compared to experimental data [42, 43]. However, the indirect nature of band gap is consistent in theory and experiments. It should be mentioned that our measured spectral behavior and band gap estimate of calcite are consistent with the previous result [44], while the experimental band gap value of aragonite has not been reported before.

To further examine the spectral features in the interband transition region below 26 eV, we consulted the calculated band structures and partial density of states (PDOS) results. According to PDOS results shown in Figure 4, both calcite and aragonite show similar behavior in terms of PDOS contributions from their constituent atoms. Our PDOS calculations revealed that the O-*p* states primarily contributed to the valence bands near the Fermi level, whereas C-*p*, O-*p*, and Ca-*d* states formed the conduction bands near the Fermi level in both calcite and aragonite. Here, we are interested in transitions occurring from the occupied Ca-*p* states lying at 19-20 eV below the Fermi level to the empty Ca-*d* states at 6 eV above the Fermi level. These transitions correspond to the Ca M_{23} edge.

3.2 Ca L_{23} vs. M_{23}

Similar to XAS [13], core-loss EELS is able to probe electronic structures with respect to a constituent atom species in a material, which makes the method attractive to differentiate polymorphs of the same chemical compositions. Indeed, the Ca L_2 and L_3 edges have been used to study not just calcite and aragonite but also other calcium compounds such as calcium phosphate,

calcium fluoride, etc [15, 45, 46]. Similar to $3d$ transition metal compounds, the involvement of $2p$ to $3d$ states make the spectral features in the Ca L edges strongly influenced by atomic multiplet and crystal field effects [17]. Meanwhile, despite being rarely studied [47], Ca M_{23} edge involves transitions from $3p$ to $3d$ states, which share the same final $3d$ states as the L edges. Therefore, the Ca M_{23} edge should also be able to be used to differentiate calcite, aragonite, and other calcium compounds, especially the difference in bonding state. In order to explore the feasibility of the M_{23} edge, we first start our discussion with the widely studied L edges to examine how their spectral features are affected by the two mentioned effects before introducing the M_{23} edge results.

Ca^{2+} in the two carbonate forms discussed here is a closed shell system that has a ground state electron configuration of $1s^2 2s^2 2p^6 3s^2 3p^6$ ($3d^0$) and its L and M edges involve the final configurations of $2p^5 \rightarrow 3d^1$ and $3p^5 \rightarrow 3d^1$, respectively. Assuming Ca^{2+} is isolated and free from its neighboring carbon and oxygen in the crystals, atomic multiplet analysis and dipole selection rule ($\Delta J = \pm 1$) lead to three available final states with their term symbols 3D_1 , 1P_1 and 3P_1 . These states can be observed in both XAS and EELS data, although the peak intensity of 3D_1 is at least one order of magnitude smaller than the other two [15, 45, 46]. As shown in Figure 5, the 3D_1 in both calcite and aragonite manifests itself as the small pre-peak feature, below the L_2 and L_3 edges, respectively. In addition to the atomic multiplet effect described in the isolated atomic scenario, the Ca atoms in both calcite and aragonite are subject to electrostatic interactions from the neighboring oxygen/carbonate anions, which lead to the crystal field effect causing the splitting of the three atomic multiplet states. The splitting is also illustrated in Figure 5, where the L_3 splits into a_1 and a_2 , and the L_2 splits into b_1 and b_2 . However, the low intensities of the pre-peak (3D_1) features make their splitting hard to observe. Our EELS results of Ca L edges are consistent with the XAS results (dotted curves) previously reported by Ref. [15]. It should be noted that neither L_3

nor L_2 edge spectra of calcite and aragonite can fully resemble the calculated Ca- d PDOS shown in Figure 4, especially with respect to the detail of crystal field splitting. It is because the atomic multiplet effect is significant and overpowers the solid state effects predicted by DFT calculations [17].

With the basic understanding of the spectral features of L edges, we now move on to analyze the M edge results. First, we note that the spin-orbit coupling is much reduced for a $3p$ orbital as compared to a $2p$ orbital for light transition metals such as titanium, which in turn reduces the atomic multiplet effect [17]. This makes the intensities of 3D_1 and 1P_1 states more than two orders of magnitude smaller in the M edge than in the L edge. As a result, only one level, M_{23} , is observed instead of two separate M_2 and M_3 [48]. Without the significant influence of the atomic multiplet effect, the remaining M_{23} edge is then primarily modified by the crystal field effect, which is captured in the PDOS of Ca- d by the DFT calculations, shown in Figure 4. The crystal field effect originates from the electrostatic interaction between the metal cation and its surrounding anion arrangement. The magnitude and structure of crystal field splitting therefore depend on the atomic species and local point group symmetry which are unique to a given crystal structure and can serve as a key differentiating feature for the identification of the bonding states in CaCO_3 polymorphs studied here.

Figures 6a and c show the comparison between the measured M_{23} spectra and calculated PDOS of Ca- d for calcite and aragonite, respectively. In calcite, each Ca atom bonds with the neighboring six oxygen atoms which form corner-sharing Ca-O octahedra showing a D_{3d} point group symmetry, as shown in Figure 6b. Within the D_{3d} point group, a five-fold degenerate Ca- d level splits into two doubly-degenerate E_g and one nondegenerate A_{1g} symmetry representations. Analysis of the Kohn-Sham energy levels at the zone center (Γ) confirms such type of energy splitting in calcite.

Our DFT calculations revealed that Ca- d_{xy} and Ca- $d_{x^2-y^2}$ orbitals comprised the lowest-energy configuration to form a doublet of E_g symmetry. This is because the Ca- d_{xy} and Ca- $d_{x^2-y^2}$ orbitals do not directly interact with the neighboring oxygen atoms which form the Ca-O octahedron, as shown in Figure 6b. Next is the nondegenerate Ca- d_{z^2} state (A_{1g}) within the middle-energy configuration. Although this orbital does not directly face the oxygen atoms, it is affected by the crystal field effect induced by the oxygen triangles of the Ca-O octahedron. Lastly, the Ca- d_{xy} and Ca- d_{yz} orbitals comprise the highest-energy doublet configuration of E_g symmetry (labeled as E'_g for distinction). These orbitals directly interact with the neighboring oxygen atoms forming the Ca-O octahedron. Our DFT calculations predicted the energy gaps of 0.72 and 1.47 eV between the $A_{1g} - E_g$ and $E'_g - A_{1g}$ levels, respectively (see Figure 6b). This is in good agreement with our EELS measurements: $A_{1g} - E_g = 0.85 \pm 0.14$ eV and $E'_g - A_{1g} = 1.55 \pm 0.14$ eV. Note that the rise of intensity with energy observed in EELS measurements in Figures 6a and c could be due to the spectral convolution with the inelastic scattering cross-section profile of the M edge. And the ‘delay maximum’ around 35 eV observed in Figure 2 is due to a centrifugal-barrier effect [13, 47, 49, 50].

In aragonite, the crystal-field splitting is more complex due to lower symmetry of Ca-O dodecahedron compared to that in calcite. In aragonite, one Ca atom bonds with nine neighboring oxygen atoms, which forms a complex polyhedron showing a D_{2h} point group symmetry. The neighboring polyhedra are connected with both edge and corner sharing, as shown in Figure 6d. Within the D_{2h} point group, a five-fold degenerate Ca- d level splits into five nondegenerate levels, named as A_g and B_{ig} ($i = 1, 2, 3$) symmetry representations. The Ca- d_{xy} , Ca- d_{yz} and Ca- d_{xz} states correspond to the B_{1g} , B_{3g} and B_{2g} representations, respectively, whereas both Ca- d_{z^2} and Ca- $d_{x^2-y^2}$ states belong to the A_g representation. Since there are four Ca-O polyhedra in a unit cell

which tilt along different orientations and share with edges and corners, the average crystal-field splitting between the states of the three B_g representations is small and the distinct B_g states from different Ca-O polyhedra nearly overlap onto each other to form a band-like feature. Similarly, the two nondegenerate A_g states also exhibit subtle energy splitting. However, there is a distinct energy gap of ~ 0.57 eV (DFT) between the B_g and A_g sub-bands, as shown in Figure 6d. This is consistent with our measured EELS spectrum shown in Figure 6c, where two convoluted peak-like features can be observed, corresponding to the A_g and B_g sub-bands, respectively.

Moreover, we noted that the role of carbon atoms on the crystal-field splitting is not significant in both calcite and aragonite. Our DFT optimized crystal structures suggest that Ca atoms form relatively stronger bonds with neighboring O atoms while much weaker bonds with neighboring C atoms in both CaCO_3 polymorphs. For example, in calcite, the DFT optimized Ca-O bond length ranges from 2.42 to 2.63 Å (anisotropic Ca-O polyhedra), whereas Ca-C bond length is about 2.90 Å. In both CaCO_3 polymorphs, Ca-C bond is about 37% (calcite) and 16% (aragonite) larger than the Ca-O bonds. Therefore, the role of C- p orbitals on the crystal-field splitting of Ca- d states can be safely considered insignificant in the two studied polymorphs.

Based on the above results, we know that the difference in bonding states between calcite and aragonite resides in their Ca M_{23} near edge fine structures starting around 26 eV that tightly relates to the final d states and crystal symmetries. More importantly, the fine spectral features from the Ca M_{23} edge allow the interpretations of PDOS obtained by DFT calculations, which is because of the much-reduced atomic multiplet effect in the $3p$ orbital. As we known, EELS are powerful to the understanding of bonding and/or oxidation states of elements in various materials [13, 47, 51-53], however, it is still challenge to interpret the experimental results as compared with theoretical predictions, especially for $3d$ transition metal elements, owing to the significant atomic multiplet

effect [17]. We provide an applicable example to investigate the bonding states of Ca element in CaCO₃ polymorphs from low-loss EELS analysis. Our Ca-*M* edge analysis is well supported from the interpretations of PDOS obtained by DFT calculations, which has been rarely reported before. Our approach from low-loss EELS definitely brings insights to the study of bonding states in many minerals or biominerals that have polymorphs, especially for those including 3*d* transition metal elements showing significant atomic multiplet effect in core-loss EELS.

3.3 Dielectric Function and Valence Plasmon

Figure 7 shows the complex dielectric functions of calcite and aragonite using the procedures described in Appendix A and Appendix B. The starting values for the refractive indices of the materials are obtained from Ref. [24]. The resulting dielectric functions reveal the intrinsic material responses and allow the scattering intensity to be compared. Due to the lack of experimental results of calcium carbonates from other methods (like optical methods), a direct evaluation of our dielectric function is not possible. However, we found one calculated dielectric function of calcite in Ref. [39]. Our experimental results are well in agreement with the theoretical prediction of calcite by DFT calculations. To the best of our knowledge, we provided the first experimental data for the dielectric function of calcite and aragonite which could be important to the researchers focusing on the optical properties of calcium carbonates.

One interesting finding is the unusual plasmon behavior in the dielectric function results, that is the absence of valence plasmon signature – the zero-crossing of ϵ_1 with a positive slope – in both calcite and aragonite. This characteristic was neglected by Katti *et al.* [20] for the study of the dielectric function in CaCO₃ polymorphs. Going through the optical properties of insulator database [54], it is found that hexagonal indium nitride also does not have the zero-crossing feature in its ϵ_1 . However, similar to the free electrons in metals, valence electrons in semiconductors and

insulators should show collective behavior [13]. Using the simple free-electron model and the valence configuration of Ca $4s^2$, C $2s^2$ and O $2p^4$, one expects calcite and aragonite to have their valence plasmon energies at 19.0 and 19.7 eV, respectively. We therefore believe that the peak around 35 eV should be the delayed maximum associated to Ca M_{23} edge which is due to the centrifugal-barrier effect in $3p \rightarrow 3d$ transitions [49, 50]. And we speculate that the valence plasmon in calcite and aragonite have some kind of interactions with nearby interband transitions which cause their zero-crossing signatures disappeared in the dielectric functions.

4. Conclusion

Two most stable CaCO_3 polymorphs, calcite and aragonite, were characterized by using STEM-EELS in the valence region and DFT. The indirect band gaps of calcite and aragonite were determined experimentally to be 7.10 and 6.79 eV, respectively. The most apparent difference in bonding states between the two CaCO_3 polymorphs resides in their Ca M_{23} near edge fine structures starting around 26 eV that tightly relates to the final d states and crystal symmetries. The fine structures from the Ca M_{23} edge allow the interpretations of PDOS obtained by DFT calculations, which is because of the much-reduced atomic multiplet effect in the $3p$ orbital. Our findings show insights that PDOS has great potential for the interpretation of M_{23} edge spectrum from lighter $3d$ transition metals such as scandium, titanium, vanadium and chromium in which such interpretation may not be achieved for their L edges.

Acknowledgements

We thank H. Yang and M. Hoffman for discussions regarding the optical configuration of the microscope. First-principles calculations were performed using the computational resources provided by the Rutgers University Parallel Computing clusters. This work was supported by the

U.S. Department of Energy (DOE), Office of Science, Basic Energy Sciences under awards DE-SC0020353 (S. Singh) and DE-SC0005132 (P. Batson). S.S. and K.M.R. acknowledge the support from the Office of Naval Research (ONR) grant N00014-21-1-2107. D.V. acknowledges the support from National Science Foundation grant DMR-1954856. The authors acknowledge the use of Princeton's Imaging and Analysis Center, which is partially supported by the Princeton Center for Complex Materials, a National Science Foundation (NSF)-MRSEC program (DMR-2011750).

Declaration of Competing Interest

The authors declare that they have no known competing financial interests or personal relationships that could have appeared to influence the work reported in this paper.

Appendix A. Valence Loss Spectroscopy and Energy-Loss Function

EELS probes transitions from initial occupied to final unoccupied states in a material, which means that beyond basic element identification work, EELS can also be utilized to study the electronic and optical properties of the material [13, 55, 56] by analyzing the spectral features that occur in the low energy-loss (< 50 eV) region. According to the dielectric formalism and in the absence of plural scattering, the acquired single scattering EELS distribution (SSD) is linked to its corresponding energy-loss function (ELF), $Im\left(\frac{-1}{\varepsilon(E)}\right)$ [13], through the following relation:

$$SSD(E) = \frac{2I_0 t}{\pi a_0 m_0 v^2} Im\left(\frac{-1}{\varepsilon(E)}\right) \ln\left[1 + \left(\frac{\beta}{\theta_E}\right)^2\right] \quad (\text{A.1})$$

where I_0 , a_0 , m_0 , v , $\varepsilon(E)$, β , and θ_E are the zero-loss intensity, Bohr radius, electron rest mass, the incident electron speed, the dielectric function of the material, the collection semi-angle, and the characteristic scattering angle, respectively. Assuming the inelastic scattering events follow

Poisson statistics, the SSD can be obtained by applying Fourier-log deconvolution to the as acquired spectrum.

Appendix B. Dielectric Function and Kramers-Kronig Relation

The experimentally measured ELF contains the imaginary part of the dielectric function, and the real part can be obtained by applying the Kramers-Kronig relation:

$$Re \left[\frac{1}{\varepsilon(E)} \right] - 1 = \frac{-P}{\pi} \int_{-\infty}^{\infty} \frac{ELF(E')}{E' - E} dE' \quad (\text{B.1})$$

where P is the Cauchy principal part of the integral [13, 57]. The dielectric response of a material is assumed to obey causality where the material is not disturbed before an external perturbation occurs. Utilizing causality, it can be shown that the real and imaginary parts of the dielectric function are related to even and odd parts of time-dependent response without actually working out the Cauchy principal value as follows [58, 59]:

$$\begin{cases} q(t) = FT^{-1} \left\{ -i \times Im \left[\frac{-1}{\varepsilon(E)} \right] \right\} \\ p(t) = sgn(t)q(t) \\ p(t) = FT^{-1} \left\{ Re \left[\frac{1}{\varepsilon(E)} \right] - 1 \right\} \end{cases} \quad (\text{B.2})$$

where $q(t)$ is related to the inverse Fourier transform of the measured energy-loss function, which represents the odd part of the time-dependent response function. $p(t)$ represents the even part of the time-dependent response function and is related to the real part of the dielectric function. $q(t)$ and $p(t)$ are related by the signum function $sgn(t)$. The complex dielectric function, $\varepsilon(E)$, of the material is then worked out as follows:

$$\varepsilon(E) = \varepsilon_1(E) + i\varepsilon_2(E) = \frac{Re \left[\frac{1}{\varepsilon(E)} \right] + iIm \left[\frac{-1}{\varepsilon(E)} \right]}{\left\{ Re \left[\frac{1}{\varepsilon(E)} \right] \right\}^2 + \left\{ Im \left[\frac{-1}{\varepsilon(E)} \right] \right\}^2} \quad (4)$$

References

- [1] Y. Politi, R.A. Metzler, M. Abrecht, B. Gilbert, F.H. Wilt, I. Sagi, L. Addadi, S. Weiner, P. Gilbert, Transformation mechanism of amorphous calcium carbonate into calcite in the sea urchin larval spicule, *Proceedings of the National Academy of Sciences* 105 (2008) 17362-17366.
- [2] I.A. Aksay, M. Trau, S. Manne, I. Honma, N. Yao, L. Zhou, P. Fenter, P.M. Eisenberger, S.M. Gruner, Biomimetic pathways for assembling inorganic thin films, *Science* 273 (1996) 892-898.
- [3] X. San, M. Gong, J. Wang, X. Ma, R. Dos Reis, P.J. Smeets, V.P. Dravid, X. Hu, Uncovering the crystal defects within aragonite CaCO_3 , *Proceedings of the National Academy of Sciences* 119 (2022) e2122218119.
- [4] M. Chaussemier, E. Pourmohtasham, D. Gelus, N. Pécoul, H. Perrot, J. Lédion, H. Cheap-Charpentier, O. Horner, State of art of natural inhibitors of calcium carbonate scaling. A review article, *Desalination* 356 (2015) 47-55.
- [5] R.A. Metzler, M. Abrecht, R.M. Olabisi, D. Ariosa, C.J. Johnson, B.H. Frazer, S.N. Coppersmith, P. Gilbert, Architecture of columnar nacre, and implications for its formation mechanism, *Physical Review Letters* 98 (2007) 268102.
- [6] D.E. Aspnes, *Handbook of optical constants of solids*. San Diego: Academic Press, 1997.
- [7] H.D. Espinosa, A.L. Juster, F.J. Latourte, O.Y. Loh, D. Gregoire, P.D. Zavattieri, Tablet-level origin of toughening in abalone shells and translation to synthetic composite materials, *Nature communications* 2 (2011) 173.
- [8] U.G. Wegst, H. Bai, E. Saiz, A.P. Tomsia, R.O. Ritchie, Bioinspired structural materials, *Nature materials* 14 (2015) 23-36.
- [9] T. Kato, A. Sugawara, N. Hosoda, Calcium carbonate–organic hybrid materials, *Advanced Materials* 14 (2002) 869-877.
- [10] L. Collins, M. Naeni, F. Schäfer, C. Brignoli, A. Schiavi, J. Roberts, P. Colgan, The effect of a calcium carbonate/perlite toothpaste on the removal of extrinsic tooth stain in two weeks, *International dental journal* 55 (2005) 179-182.
- [11] A. Joiner, Review of the extrinsic stain removal and enamel/dentine abrasion by a calcium carbonate and perlite containing whitening toothpaste, *International dental journal* 56 (2006) 175-180.
- [12] F.M. Hossain, G.E. Murch, I.V. Belova, B.D. Turner, Electronic, optical and bonding properties of CaCO_3 calcite, *Solid state communications* 149 (2009) 1201-1203.
- [13] R.F. Egerton, *Electron energy-loss spectroscopy in the electron microscope*: Springer Science & Business Media, 2011.
- [14] R.A. Metzler, P. Rez, Polarization dependence of aragonite calcium L-edge XANES spectrum indicates c and b axes orientation, *The Journal of Physical Chemistry B* 118 (2014) 6758-6766.
- [15] P. Rez, A. Blackwell, Ca L23 spectrum in amorphous and crystalline phases of calcium carbonate, *The Journal of Physical Chemistry B* 115 (2011) 11193-11198.
- [16] U. Golla-Schindler, G. Benner, A. Orchowski, U. Kaiser, In situ observation of electron beam-induced phase transformation of CaCO_3 to CaO via ELNES at low electron beam energies, *Microscopy and microanalysis* 20 (2014) 715-722.
- [17] F. de Groot, Multiplet effects in X-ray spectroscopy, *Coordin Chem Rev* 249 (2005) 31-63.

- [18] G. Cheng, S. Yao, X. Sang, B. Hao, D. Zhang, Y.K. Yap, Y. Zhu, Evolution of Irradiation-Induced Vacancy Defects in Boron Nitride Nanotubes, *Small* 12 (2016) 818-824.
- [19] G. Ghosh, Dispersion-equation coefficients for the refractive index and birefringence of calcite and quartz crystals, *Optics Communications* 163 (1999) 95-102.
- [20] K.S. Katti, M. Qian, D.W. Frech, M. Sarikaya, Low-loss electron energy-loss spectroscopy and dielectric function of biological and geological polymorphs of CaCO₃, *Microscopy and Microanalysis* 5 (1999) 358-364.
- [21] V. Srot, U.G.K. Wegst, U. Salzberger, C.T. Koch, K. Hahn, P. Kopold, P.A. van Aken, Microstructure, chemistry, and electronic structure of natural hybrid composites in abalone shell, *Micron* 48 (2013) 54-64.
- [22] M. Stöger-Pollach, H. Franco, P. Schattschneider, S. Lazar, B. Schaffer, W. Grogger, H. Zandbergen, Čerenkov losses: A limit for bandgap determination and Kramers–Kronig analysis, *Micron* 37 (2006) 396-402.
- [23] N. Brodusch, H. Demers, A. Gellé, A. Moores, R. Gauvin, Electron energy-loss spectroscopy (EELS) with a cold-field emission scanning electron microscope at low accelerating voltage in transmission mode, *Ultramicroscopy* 203 (2019) 21-36.
- [24] W.L. Bragg, The refractive indices of calcite and aragonite, *Proceedings of the Royal Society of London. Series A, Containing Papers of a Mathematical and Physical Character* 105 (1924) 370-386.
- [25] N. Sakaguchi, L. Tanda, Y. Kunisada, Measurement of the dielectric function of α -Al₂O₃ by transmission electron microscopy–Electron energy-loss spectroscopy without Čerenkov radiation effects, *Ultramicroscopy* 169 (2016) 37-43.
- [26] G. Cheng, C. Miao, Q. Qin, J. Li, F. Xu, H. Haftbaradaran, E.C. Dickey, H. Gao, Y. Zhu, Large anelasticity and associated energy dissipation in single-crystalline nanowires, *Nature Nanotechnology* 10 (2015) 687-691.
- [27] R. Erni, N.D. Browning, The impact of surface and retardation losses on valence electron energy-loss spectroscopy, *Ultramicroscopy* 108 (2008) 84-99.
- [28] M. Stöger-Pollach, A. Laister, P. Schattschneider, Treating retardation effects in valence EELS spectra for Kramers–Kronig analysis, *Ultramicroscopy* 108 (2008) 439-444.
- [29] Q. Meng, L. Wu, H.L. Xin, Y. Zhu, Retrieving the energy-loss function from valence electron energy-loss spectrum: Separation of bulk-, surface-losses and Čerenkov radiation, *Ultramicroscopy* 194 (2018) 175-181.
- [30] G. Kresse, J. Furthmüller, Efficient iterative schemes for ab initio total-energy calculations using a plane-wave basis set, *Physical review B* 54 (1996) 11169.
- [31] G. Kresse, J. Furthmüller, Efficiency of ab-initio total energy calculations for metals and semiconductors using a plane-wave basis set, *Computational materials science* 6 (1996) 15-50.
- [32] G. Kresse, D. Joubert, From ultrasoft pseudopotentials to the projector augmented-wave method, *Physical review b* 59 (1999) 1758.
- [33] J.P. Perdew, A. Ruzsinszky, G.I. Csonka, O.A. Vydrov, G.E. Scuseria, L.A. Constantin, X. Zhou, K. Burke, Restoring the density-gradient expansion for exchange in solids and surfaces, *Physical review letters* 100 (2008) 136406.
- [34] U. Herath, P. Tavazze, X. He, E. Bousquet, S. Singh, F. Muñoz, A.H. Romero, PyProcar: A Python library for electronic structure pre/post-processing, *Computer Physics Communications* 251 (2020) 107080.

- [35] E. Maslen, V. Streltsov, N. Streltsova, N. Ishizawa, Electron density and optical anisotropy in rhombohedral carbonates. III. Synchrotron X-ray studies of CaCO₃, MgCO₃ and MnCO₃, *Acta Crystallographica Section B: Structural Science* 51 (1995) 929-939.
- [36] B. Dickens, J. Bowen, Refinement of the crystal structure of the aragonite phase of CaCO₃, *Journal of Research of the National Bureau of Standards. Section A, Physics and Chemistry* 75 (1971) 27.
- [37] B. Rafferty, L. Brown, Direct and indirect transitions in the region of the band gap using electron-energy-loss spectroscopy, *Physical Review B* 58 (1998) 10326.
- [38] M. Brik, First-principles calculations of structural, electronic, optical and elastic properties of magnesite MgCO₃ and calcite CaCO₃, *Physica B: Condensed Matter* 406 (2011) 1004-1012.
- [39] S. Medeiros, E. Albuquerque, F. Maia, E. Caetano, V. Freire, Electronic and optical properties of CaCO₃ calcite, and excitons in Si@ CaCO₃ and CaCO₃@ SiO₂ core-shell quantum dots, *Journal of Physics D: Applied Physics* 40 (2007) 5747.
- [40] S. Medeiros, E. Albuquerque, F. Maia Jr, E. Caetano, V. Freire, Structural, electronic, and optical properties of CaCO₃ aragonite, *Chemical physics letters* 430 (2006) 293-296.
- [41] A.J. Skinner, J.P. LaFemina, H.J. Jansen, Structure and bonding of calcite: a theoretical study, *American Mineralogist* 79 (1994) 205-214.
- [42] J.P. Perdew, Density functional theory and the band gap problem, *International Journal of Quantum Chemistry* 28 (1985) 497-523.
- [43] B. Pedro, J. Schmidt, A.W. Huran, F. Tran, M.M. AL, B. Silvana, Exchange-correlation functionals for band gaps of solids: benchmark, reparametrization and machine learning, *npj Computational Mater.* 6 (2020).
- [44] M. Vos, G. Marmitt, Y. Finkelstein, R. Moreh, Determining the band gap and mean kinetic energy of atoms from reflection electron energy loss spectra, *The Journal of chemical physics* 143 (2015) 104203.
- [45] S. Naftel, T. Sham, Y. Yiu, B. Yates, Calcium L-edge XANES study of some calcium compounds, *Journal of synchrotron radiation* 8 (2001) 255-257.
- [46] F. de Groot, J. Fuggle, B. Thole, G. Sawatzky, L 2, 3 x-ray-absorption edges of d 0 compounds: K⁺, Ca 2⁺, Sc 3⁺, and Ti 4⁺ in O h (octahedral) symmetry, *Physical Review B* 41 (1990) 928.
- [47] F. Hofer, P. Wilhelm, EELS microanalysis of the elements Ca to Cu using M23 edges, *Ultramicroscopy* 49 (1993) 189-197.
- [48] B.L. Henke, E.M. Gullikson, J.C. Davis, X-ray interactions: photoabsorption, scattering, transmission, and reflection at E= 50-30,000 eV, Z= 1-92, *Atomic data and nuclear data tables* 54 (1993) 181-342.
- [49] S.T. Manson, J.W. Cooper, Photo-Ionization in the Soft x-Ray Range: 1 Z Dependence in a Central-Potential Model, *Physical Review* 165 (1968) 126.
- [50] R. Leapman, P. Rez, D. Mayers, K, L, and M shell generalized oscillator strengths and ionization cross sections for fast electron collisions, *The Journal of Chemical Physics* 72 (1980) 1232-1243.
- [51] C. Colliex, From early to present and future achievements of EELS in the TEM, *The European Physical Journal Applied Physics* 97 (2022) 38.
- [52] X. Song, R. Singha, G. Cheng, Y.-W. Yeh, F. Kamm, J.F. Khoury, B.L. Hoff, J.W. Stiles, F. Pielnhofer, P.E. Batson, Synthesis of an aqueous, air-stable, superconducting 1T'-WS₂ monolayer ink, *Science Advances* 9 (2023) eadd6167.

- [53] X. Song, G. Cheng, D. Weber, F. Pielhofer, S. Lei, S. Klemenz, Y.-W. Yeh, K.A. Filsinger, C.B. Arnold, N. Yao, L.M. Schoop, Soft Chemical Synthesis of HxCrS₂: An Antiferromagnetic Material with Alternating Amorphous and Crystalline Layers, *Journal of the American Chemical Society* 141 (2019) 15634-15640.
- [54] S. Adachi, *Optical constants of crystalline and amorphous semiconductors : numerical data and graphical information*. Boston: Kluwer Academic Publishers, 1999.
- [55] F.G. de Abajo, Optical excitations in electron microscopy, *Reviews of modern physics* 82 (2010) 209.
- [56] A.P. Hitchcock, Near edge electron energy loss spectroscopy: Comparison to x-ray absorption, *Japanese Journal of Applied Physics* 32 (1993) 176.
- [57] J. Daniels, C.v. Festenberg, H. Raether, K. Zeppenfeld, *Optical constants of solids by electron spectroscopy*. Springer Tracts in Modern Physics, Volume 54. Springer, 1970. p.77-135.
- [58] D. Johnson, A Fourier series method for numerical Kramers-Kronig analysis, *Journal of Physics A: Mathematical and General* 8 (1975) 490.
- [59] C. Li, G. Subramanian, J.C. Spence, Time-resolved spectra from millivolt EELS data, *Microscopy and Microanalysis* 20 (2014) 837-846.

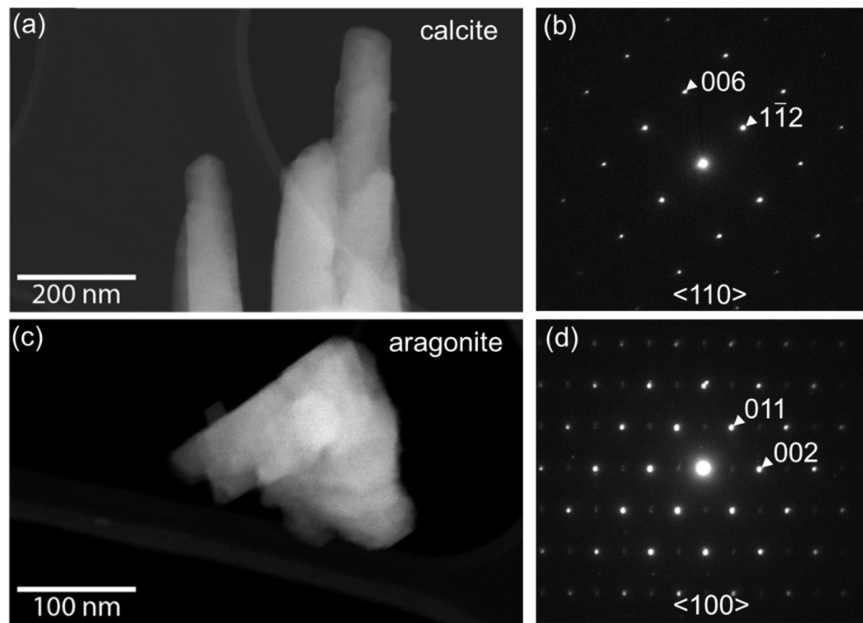


Figure 1. High angle annular dark field images showing typical appearances of calcite (a) and aragonite (c) particles. Their corresponding diffraction patterns are shown in (b) and (d), taken from $\langle 110 \rangle$ and $\langle 100 \rangle$ zone axes, respectively.

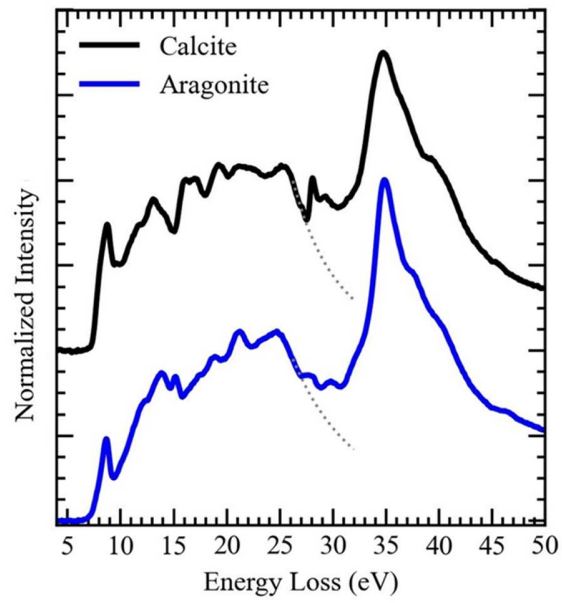


Figure 2. Valence-loss spectra of calcite (black) and aragonite (blue). The grey dotted lines are the pow-law estimated background levels for the subsequent Ca M_{23} edge extraction step.

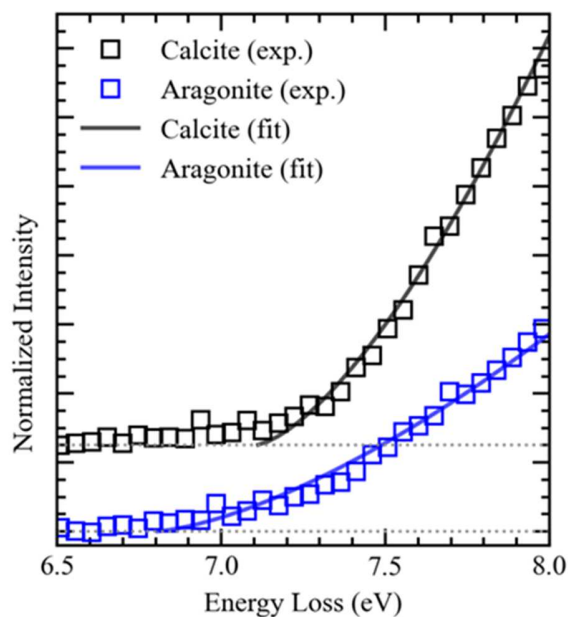


Figure 3. Measured band gap onset region of calcite (hollow black squares) and aragonite (hollow blue squares). Both calcite and aragonite show indirect gap behavior, where the onset intensities are proportional to $(E - E_g)^{1.5}$, as indicated by the black and blue fitted curves, respectively. The band gaps for calcite and aragonite were measured to be about 7.10 and 6.79 eV, respectively.

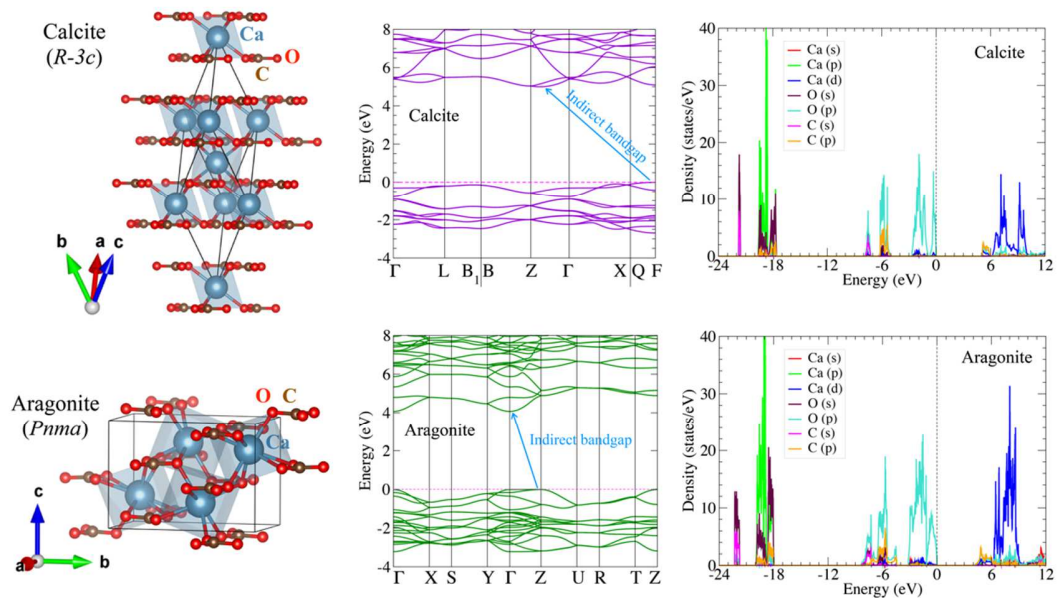


Figure 4. Calculated electronic band structure and partial density of states for calcite (top row) and aragonite (bottom row). The Fermi level (marked by dashed magenta line) was set at the valence band maximum.

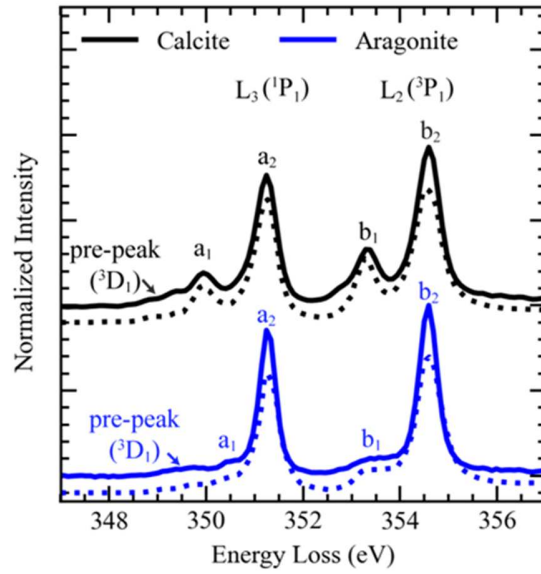


Figure 5. EELS Ca L edge spectra of calcite (solid black) and aragonite (solid blue) and the replotted XAS data (dotted lines) from Ref. [14] for comparison. Due to the atomic multiplet effect, three final states labeled as pre-peak (3D_1), L_3 (1P_1) and L_2 (3P_1) can be observed. Each multiplet state can be further splitted due to the crystal field effect – L_3 into a_1 and a_2 , L_2 into b_1 and b_2 . Note that the pre-peak (3D_1) intensities are too low to distinguish the splitting.

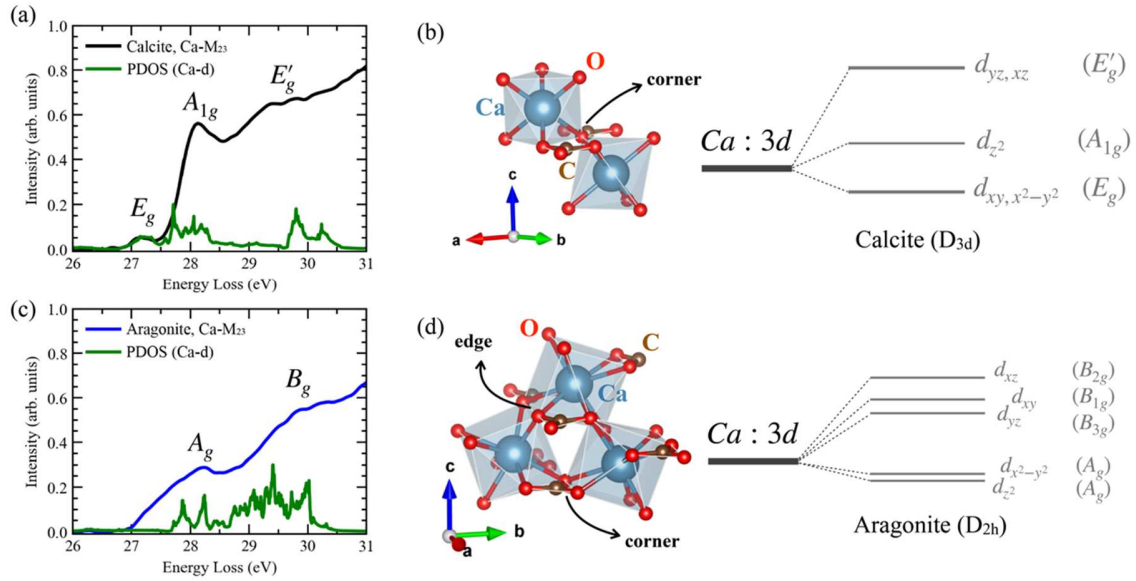


Figure 6. Measured and calculated bonding states in calcite and aragonite. (a) measured Ca M_{23} edge against calculated PDOS for Ca- d states and (b) atomic arrangement and the corresponding symmetry-governed crystal-field splitting of Ca- d states for calcite. (c) and (d) are the equivalent sets but for aragonite. Note that the energy levels shown in panels (b, d) were estimated from the DFT-calculated Kohn-Sham energy eigenvalues at the zone center (Γ).

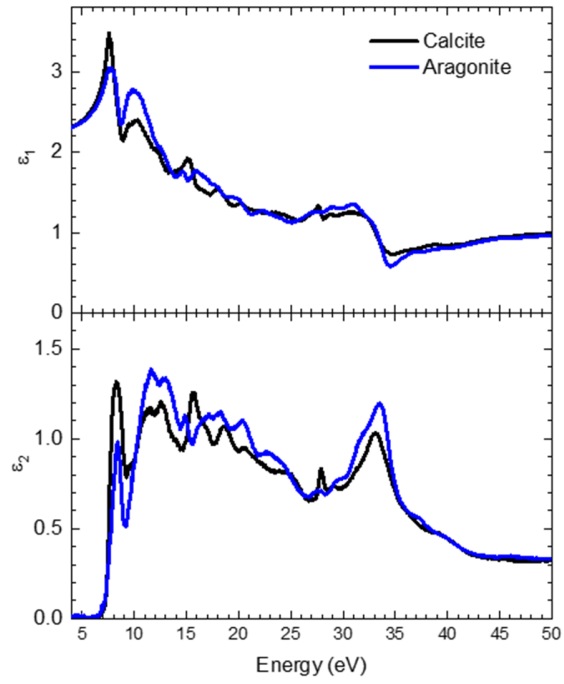
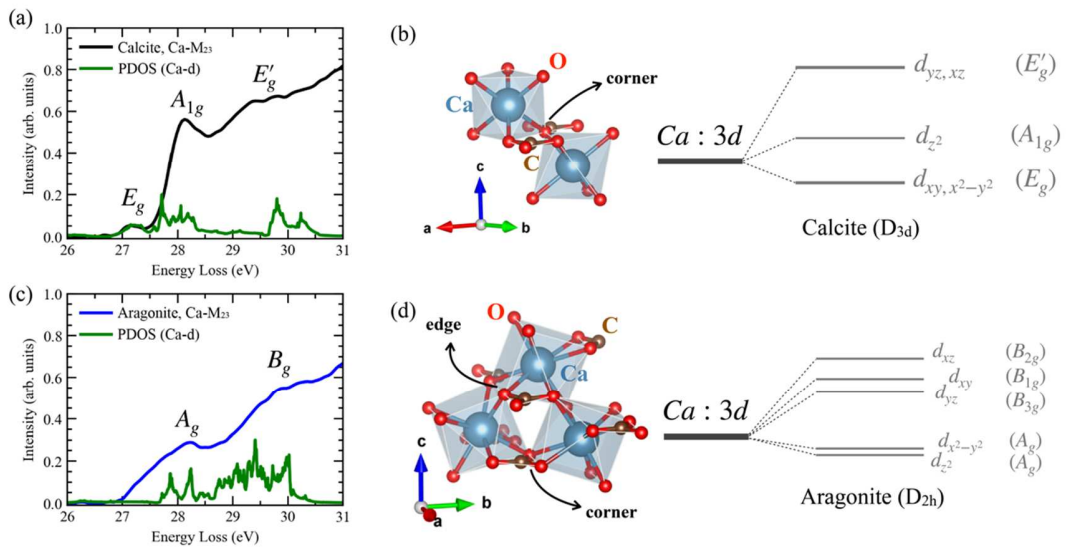


Figure 7. Real (ϵ_1) and imaginary (ϵ_2) parts of calcite (black) and aragonite's (blue) dielectric functions.

Graphic Abstract



The structural differences in calcite (top row) and aragonite (bottom row) lead to different crystal-field induced final Ca $3d$ states. The final states are characterized by Ca M_{23} edge with EELS and partial density of states (a and c) and illustrated graphically (b and d). It is noted that such density of states interpretation is often not possible with higher energy L edges of transition metals including Ca. See the manuscript for more details.